# Identifying the sensitive areas in targeted observation for predicting the Kuroshio large meander path in a regional ocean model

Xia Liu[1], Qiang Wang[2, 3*], Mu Mu[4]

[1] School of Mathematics, Zhengzhou University of Aeronautics, Zhengzhou 450046, China

[2] Key Laboratory of Marine Hazards Forecasting of Ministry of Natural Resources, Hohai University, Nanjing 210098, China

[3] College of Oceanography, Hohai University, Nanjing 210098, China

[4] Institute of Atmospheric Sciences, Fudan University, Shanghai 200438, China

**Abstract**

With the Regional Ocean Modeling System (ROMS), this paper investigates the sensitive areas in targeted observation for predicting the Kuroshio large meander (LM) path using the conditional nonlinear optimal perturbation approach. To identify the sensitive areas, the optimal initial errors (OIEs) featuring the largest nonlinear evolution in the LM prediction are first calculated; the resulting OIEs are localized mainly in the upper 2 500 m over the LM upstream region, and their spatial structure has certain similarities with that of the optimal triggering perturbation. Based on this spatial structure, the sensitive areas are successfully identified, located southeast of Kyushu in the region (29°–32°N, 131°–134°E). A series of sensitivity experiments indicate that both the positions and the spatial structure of initial errors have important effects on the LM prediction, verifying the validity of the sensitive areas. Then, the effect of targeted observation in the sensitive areas is evaluated through observing system simulation experiments. When targeted observation is implemented in the identified sensitive areas, the prediction errors are effectively reduced, and the prediction skill of the LM event is improved significantly. This provides scientific guidance for ocean observations related to enhancing the prediction skill of the LM event.

**Key words:** Kuroshio large meander, targeted observation, sensitive areas, ROMS

---

## 1 Introduction

The Kuroshio, the well-known western boundary current of the North Pacific Ocean, exhibits remarkable bimodal states when it flows through the southern region of Japan; these two states are known as the large meander (LM) path and the non-large meander (NLM) path (Taft, 1972; Kawabe, 1995). The Kuroshio path variations between these two states have important impacts on the local climate, fishery distribution, and maritime safety (Shao et al., 2005; Xu et al., 2010; Nakamura et al., 2012; Hayasaki et al., 2013). Hence, it is vital to accurately predict the path state of the Kuroshio. However, many factors, such as limitations in numerical models and a lack of observation data and the dynamic mechanism of Kuroshio path variations (Ma et al., 2016), may lead to uncertainties in the LM prediction results. To reduce the prediction uncertainties, it is important to investigate the predictability of Kuroshio path variations.

Studies have pointed out that uncertainties in initial conditions are an important cause of LM prediction uncertainties (Ishikawa et al., 2004; Miyazawa et al., 2005; Fujii et al., 2008;

Wang et al., 2012). Recent research on the effects of initial conditions on LM prediction has focused on two main aspects: one involves investigation of the initial perturbation that is most likely to result in the LM path, also called the optimal triggering perturbation (OTP) of the LM event in this study; the other involves exploration of the initial errors causing the largest prediction uncertainties under the given initial constraint condition, also called the optimal initial errors (OIEs) in LM prediction. Some progress has been made regarding both of these aspects. For example, Wang et al. (2013a, b) investigated the OTP of the LM event and the OIEs in a 1.5-layer shallow-water model using the conditional nonlinear optimal perturbation (CNOP) approach, and revealed similarities between the OIEs and OTP. However, their model is too simple to consider the effects of baroclinic processes and topography. To overcome this limitation, Liu et al. (2018a) adopted the Regional Ocean Modeling System (ROMS) and the CNOP approach to explore the OTP of the LM event and its evolution mechanism, thereby confirming the importance of nonlinear physical processes in the LM formation process. De-

termining the triggering signal of the LM event can help us to better understand the physical mechanism responsible for the LM path and thereby contribute to predicting the LM path. However, the OIEs existing in the LM prediction will contaminate the prediction results and greatly suppress the LM prediction skill. Therefore, exploring OIEs will deepen our understanding of prediction uncertainties. Liu et al. (2018b) used the simulated LM formation process as the background state to explore the OIEs and their growth mechanism, but the parameter setting and calculation conditions were different from Liu et al. (2018a). To eliminate the effect of these factors, this paper adopts the LM formation process triggered by the OTP as a new background state to search for the OIEs in the LM prediction. In this way, this study can not only exclude the influence of model parameters and model errors, but also provide conditions for investigating the links between the OIEs and the OTP. The comparison between OIEs and OTP will contribute to identifying the sensitive areas in targeted observation for predicting the Kuroshio LM path.

For numerical predictions in recent years, data assimilation has been commonly used to obtain better initial conditions (Tang et al., 2004; Farrara et al., 2013). However, ocean observations are expensive and cannot fully cover the vast area associated with the target event. Therefore, targeted observation (also called adaptive observation) developed after the 1990s has become a popular new observation strategy. As shown in Fig. 1, targeted observation aims to improve the prediction results in a validation area at the verification time when additional observations are performed in some key areas (namely, sensitive areas) at the target time, thereby providing a more accurate initial field for the model (Langland, 2005; Mu et al., 2009). In this way, the prediction errors are reduced by reducing the uncertainties in the initial conditions of sensitive areas, and the numerical prediction results are improved (Mu, 2013). Thus, identifying the sensitive areas is a key step of targeted observation.

Recently, Fujii et al. (2008) applied singular vector analysis to reveal that the anticyclonic eddy approaching southeastern Kyushu plays an important role in the LM formation process. This conclusion can contribute to the design of an effective observation system. However, singular vector analysis is a linear method and consequently ignores the effect of nonlinearity on the formation of the LM path. Subsequently, Zou et al. (2016) used a shallow-water model and concluded that the CNOP approach is more suitable than the singular vector method for determining the sensitive areas in targeted observation. Therefore, to overcome the limitations in the above methods and models in LM prediction, this paper adopted the ROMS and CNOP approach to investigate the sensitive areas in targeted observation. The objectives of the work were as follows: (1) to calculate the OIEs in the LM prediction, (2) to determine the sensitive areas in targeted observation for predicting the LM event, and (3) to evaluate the effect of targeted observation.
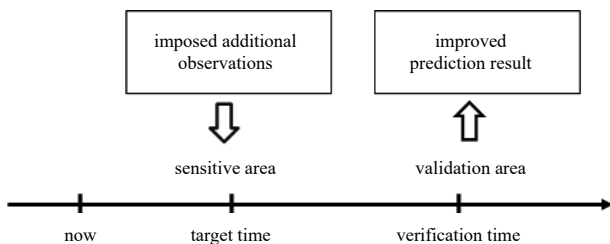
The outline of this paper is as follows. Section 2 describes the model simulation and the nonlinear optimization problem related to OIEs. In Section 3, the calculated OIEs are presented; then, based on the OIEs, the sensitive areas are identified, and the targeted observation effect is evaluated. Finally, a conclusion is presented in Section 4.

## 2 Model and method

### 2.1 *Model simulation*

Numerical experiments are performed using the ROMS model, a 3-D primitive equation ocean model that not only employs a vertical terrain-following coordinate system and horizontal generalized orthogonal curvilinear coordinate system, (Song and Haidvogel, 1994) but is also equipped with various options for advection schemes, parameterizations, and boundary conditions (Shchepetkin and McWilliams, 2003, 2005). In particular, the adjoint component of ROMS provides convenient conditions for obtaining the CNOP. In this study, considering the numerous computationally calculations, a one-way nested simulation with a 3:2 grid ratio is adopted to reproduce the Kuroshio path variations. The detailed parameter settings are presented in Table 1. With this model configuration, ROMS successfully captures the essential characteristics of the Kuroshio path variations at south of Japan presented in Liu et al. (2018b).

### 2.2 *Nonlinear optimization problem related to OIEs*

To consider the effect of nonlinearity, the CNOP approach proposed by Mu et al. (2003) is used to seek the OIEs under certain physical constraints. In this study, the nonlinear constraint optimization problem is defined as

$$J(\boldsymbol{x}_{0\delta}) = \max_{\|\boldsymbol{x}_0\|_A \leqslant \delta} J(\boldsymbol{x}_0) = \max_{\|\boldsymbol{x}_0\|_A \leqslant \delta} \|\boldsymbol{M}_t(\boldsymbol{X}_0 + \boldsymbol{x}_0) - \boldsymbol{M}_t(\boldsymbol{X}_0)\|_B^2, \quad (1)$$

where $J(\boldsymbol{x}_0) = \|\boldsymbol{M}_t(\boldsymbol{X}_0 + \boldsymbol{x}_0) - \boldsymbol{M}_t(\boldsymbol{X}_0)\|_B^2$ represents the objective function that measures the nonlinear evolution of the initial perturbation $\boldsymbol{x}_0$, $\|\boldsymbol{x}_0\|_A \leqslant \delta$ is the constraint condition, $\boldsymbol{X}_0$ is the initial state, $\boldsymbol{M}_t$ denotes the nonlinear propagator, and $\boldsymbol{x}_{0\delta}$ is the solution to the optimization problem, which is also called the CNOP. For the nonlinear optimization problem, when the NLM path is taken as the background state, the calculated CNOP is called OTP, which is most likely to result in the LM path at the prediction time. When the transition from the NLM path to the LM path is taken as the background state, the CNOPs are called OIEs, which have the largest nonlinear evolution at time $t$. This paper focuses on the OIEs existing with the OTP.

As described by Liu et al. (2018a), two cases (denoted Case 1 and Case 2) are selected herein to investigate the OTP of the LM event. By comparing the triggered LM path with the observed LM path, it is found that its formation process shares similar characteristics with the observed path (Figs 2a and b), including the strengthened recirculation gyre in the Shikoku Basin and the



**Fig. 1.** Schematic of targeted observation.

**Table 1.** Important parameters in the simulation

|                      | Nest 1                    | Nest 2                         |
| -------------------- | ------------------------- | ------------------------------ |
| Domain               | 20°S–60°N, 100°E–70°W     | 23°–46°N, 122°–162°E           |
| Resolution           | (1/8)° (~14 km)           | (1/12)° (~8 km)                |
| Boundary (open)      | WOA2009                   | model years 31–50 in Nest 1    |
| Atmospheric forcing  | COADS                     | COADS                          |
| Time step            | 300 s                     | 200 s                          |
| Spin-up              | 50 years                  | 20 years                       |
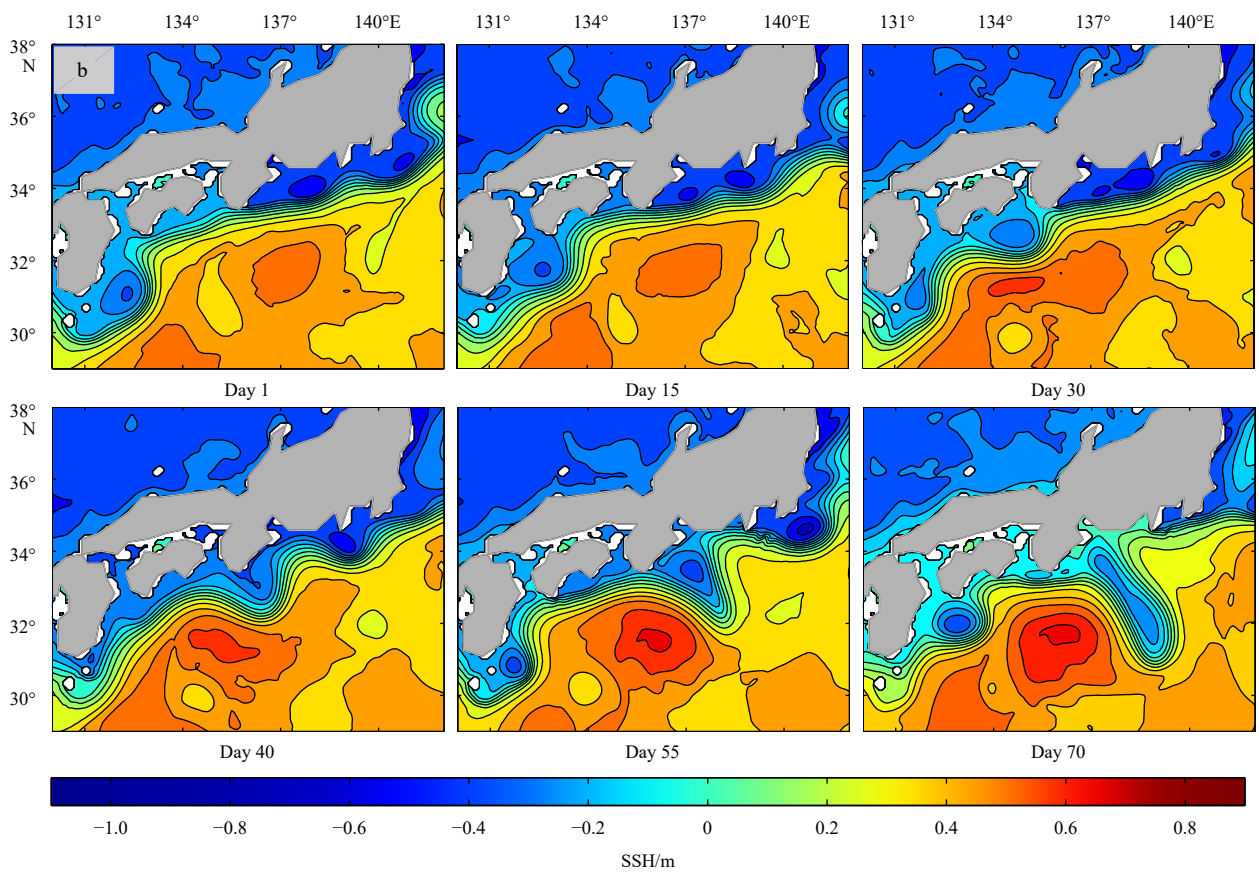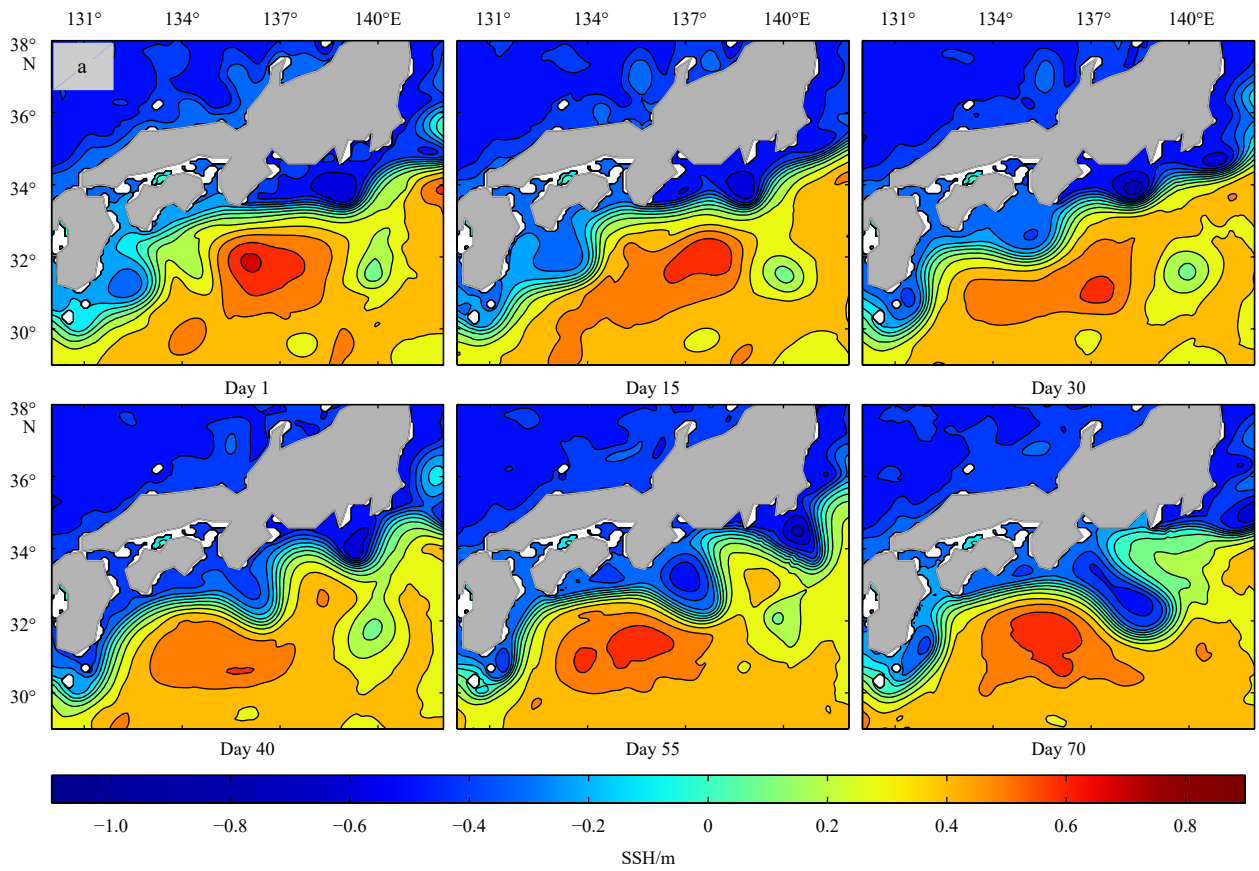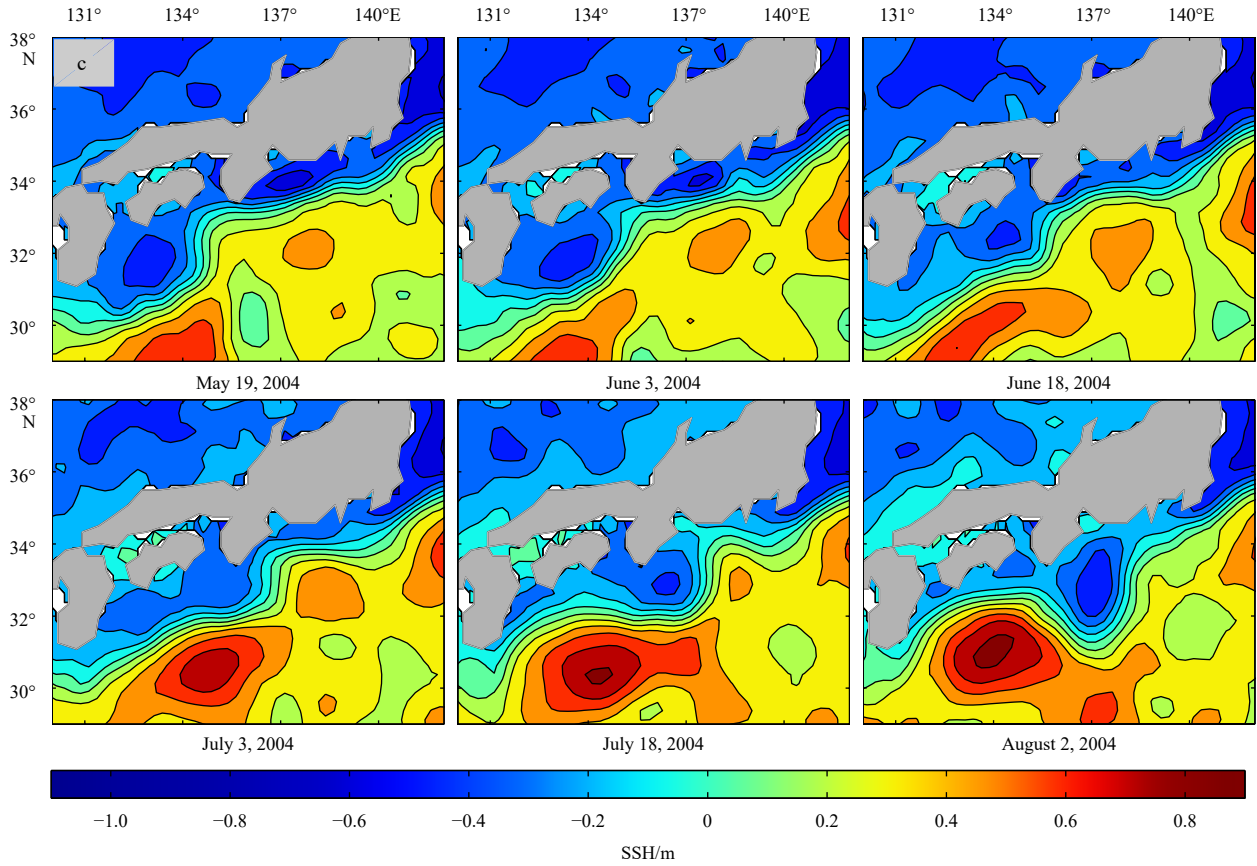
**Fig. 2.** LM formation process: induced by the OTP in Case 1 (a); induced by the OTP in Case 2 (b); observed by AVISO (c). Shading represents the sea surface height (SSH) field.

trigger meander that keeps moving downstream, although the LM path induced by the OTP extends slightly to the southeast. Therefore, it is appropriate to take the LM path triggered by the OTP as a new background state to search for the OIEs in the LM prediction.

   The parameter settings related to the calculation of the OIEs are as follows. Observation data show that the LM formation process lasts for 2-4 months and based on the model simulation (Liu et al., 2018b), the transition from the NLM path to the LM path also takes approximately 3 months. The optimization time is set to 70 days, whose dates are the same as those used to calculate the OTPs in Liu et al. (2018a). The initial time in Case 1 is September 1 in model Year 9 while Case 2 starts on November 1 in model Year 16. Similar to Li et al. (2014), the constraint norm $\|\cdot\|_A$ is selected as the sum of the quadratic errors normalized by the standard deviation. Thus, the initial error constraint not only contains the kinetic energy of the error but is also related to its potential energy and is expressed as

$$\|\boldsymbol{x}_0\|_A = \sqrt{\left(\frac{u'}{\bar{u}_{\text{std}}}\right)^2 + \left(\frac{v'}{\bar{v}_{\text{std}}}\right)^2 + \left(\frac{t'}{\bar{t}_{\text{std}}}\right)^2 + \left(\frac{s'}{\bar{s}_{\text{std}}}\right)^2 + \left(\frac{h'}{\bar{h}_{\text{std}}}\right)^2} \leqslant \delta, \tag{2}$$

where $(u', v', t', s', h')$ represent the initial errors, and $(\bar{u}_{\text{std}}, \bar{v}_{\text{std}}, \bar{t}_{\text{std}}, \bar{s}_{\text{std}}, \bar{h}_{\text{std}})$ denote the standard deviations in the upper 5 000 m within the domain (23°–46°N, 122°–162°E). They are calculated based on the monthly outputs in nest 2. $\delta$ denotes the dimensionless constraint radius. Considering the accuracy of the obser-

vational instruments and the stability of the numerical simulation, this parameter is set to $1 \times 10^7$ in this study. The norm $\|\cdot\|_B$ of the objective function is defined as the kinetic energy of the prediction errors in the upper 1 000 m over the area (25°–35°N, 135°–140°E):

$$\begin{aligned} &\|\boldsymbol{M}_t\left(\boldsymbol{X}_0 + \boldsymbol{x}_0\right) - \boldsymbol{M}_t\left(\boldsymbol{X}_0\right)\|_B^2 \\ =\ &\frac{\rho_{\text{ref}}}{2} \int\limits_{z=0}^{z=1\,000} \int\limits_{x=135°\text{E}}^{x=140°\text{E}} \int\limits_{y=25°\text{N}}^{y=35°\text{N}} \left[(u'_t)^2 + (v'_t)^2\right] \mathrm{d}x\mathrm{d}y\mathrm{d}z. \end{aligned} \tag{3}$$

   When the amplitude of the deviation from the simulated LM path in the background state is large, the objective function value is large. Moreover, the procedure of seeking the OIEs is similar to the OTP calculation although the selected background states and constraint radius are different. Readers are referred to Liu et al. (2018a) for more details.

## 3 Result

### 3.1 *OIEs in the LM prediction*

   Based on the above calculation procedure, two types of OIEs for each case are obtained, labeled CNOP1 and CNOP2. Figure 3 presents their spatial patterns, which are integrated vertically from the surface to the maximum depth according to the initial constraint form in Eq. (2). According to Fig. 3, CNOP1 and CNOP2 in the two cases are both located mainly to the southeast of Kyushu (29°32′N, 131°134′E). Examining the components of
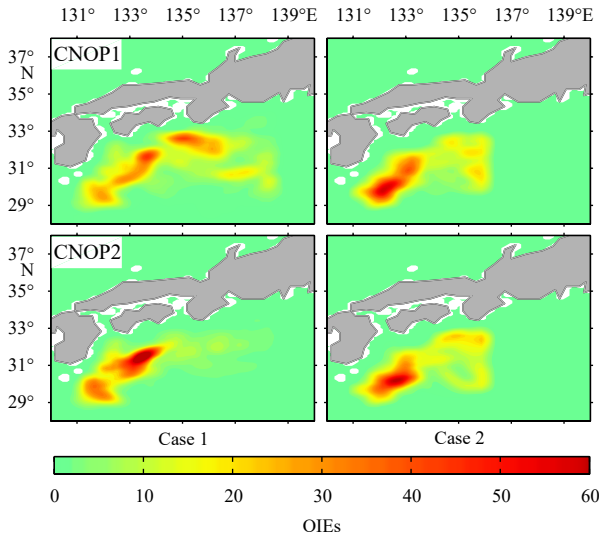
**Fig. 3.** Spatial patterns of two types of optimal initial errors (OIEs), integrated vertically from the surface to the maximum depth according to the initial constraint in Eq. (2).

the OIEs (figure not shown) demonstrates that the OIEs are concentrated mostly in the upper 2 500 m, and the spatial structures of CNOP1 and CNOP2 are slightly similar but with the opposite sign. Quantitatively, the similarity coefficients between two types of OIEs are calculated, which are defined as $S = \langle e_1, e_2 \rangle / (\|e_1\| \|e_2\|)$, in which $e_1$ and $e_2$ represent CNOP1 and CNOP2 with large amplitudes in the region (29°–32°N, 131°–134°E). They are –0.68 for Case 1 and –0.80 for Case 2. Consequently, two questions arise: why is there such a relationship between these two types of OIEs? How do they affect the LM prediction?

To explore these questions, the OIEs are superimposed onto the background states and integrate the nonlinear model forward to the prediction time. Figure 4 presents the Kuroshio axis (referring to the 16 cm isoline of the sea surface height (SSH)) at the prediction time for both Case 1 and Case 2. CNOP1 strengthens the predicted LM path, while CNOP2 weakens the LM path, and they cause the largest departure from the LM path
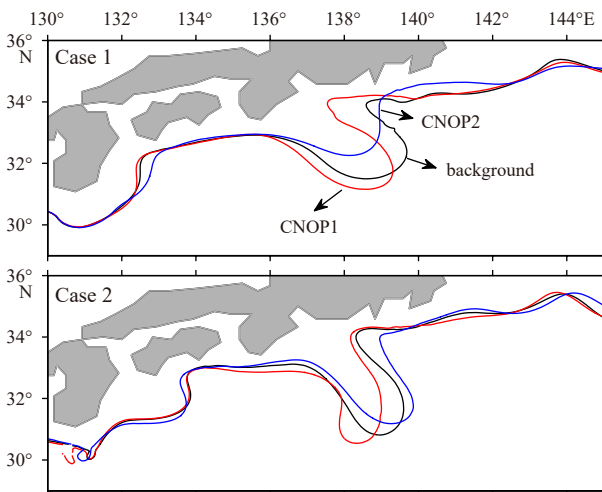


**Fig. 4.** Kuroshio axis on Day 70 in Case 1 and Case 2. The black, red, and blue lines represent the Kuroshio axes for the background state, the field with CNOP1, and the field with CNOP2, respectively.

in opposite directions at the prediction time. Additionally, Fig. 5 shows the growth of the SSH anomaly caused by the OIEs (Case 1), with the black line representing the Kuroshio axis. The non-linear evolution behavior of CNOP1 is almost opposite to that of CNOP2. Furthermore, the negative SSH anomaly of CNOP1 (Fig. 5a) gradually moves downstream along the Kuroshio axis to the region where Kuroshio path variations occur. During this process, the amplitude and intensity of the negative SSH anomaly continue to increase. Finally, its further development causes the LM path to stretch southwestward. For CNOP2 (Fig. 5b), the movement of the positive SSH anomaly downstream along the Kuroshio axis reduces the intensity of the negative anomaly, causing the LM path to be underestimated. For Case 2, a similar conclusion is obtained, but it should be noted that the OIEs are calculated with the kinetic energy of the prediction errors as the objective function. Therefore, there may be a deviation from the position of the Kuroshio axis. Moreover, it is obvious that the LM path as the background state (the black line in Fig. 4) in Case 2 is stronger than that in Case 1, which will affect the evaluation of CNOP2. Nevertheless, CNOP2 also causes the LM path to move northwest and weakens the strength of the LM path.

Through comparison with the calculated OTP of the LM path (Liu et al., 2018a), it is found that the OIEs and the OTP are both located upstream of the Kuroshio path variations, and the non-linear evolution of CNOP1 seems to be similar to that of the OTP. To further explore the links between the two, the SSH anomaly component of the OTP and OIEs in the two cases is shown in Fig. 6. Obviously, the spatial structure of CNOP1 is similar to that of the OTP, while the spatial structure of CNOP2 is exactly the opposite, which is consistent with the negative correlation between CNOP1 and CNOP2. Furthermore, the similarity coefficients between the OIEs and the OTP are calculated, which are 0.55 (–0.45) in Case 1 and 0.62 (–0.69) in Case 2. Although this calculation is affected by high-frequency signals, it shows that there exist certain similarities between the OIEs and the OTP obtained in an eddy-resolution ocean model. Therefore, it is concluded that the OIEs and the OTP in the LM prediction are localized in a relatively uniform position and that their spatial structures have similarities. The links indicate that if targeted observation is implemented, not only the initial errors are reduced, the triggering signals can also be captured, thereby improving the LM prediction skill.

### 3.2 *Identification of sensitive areas and application to targeted observation*

#### 3.2.1 *Identification of sensitive areas*

In this subsection, the sensitive areas are determined based on the spatial structures of the calculated CNOPs. Zhang et al. (2017) pointed out that the total energy is the most effective way to identify the sensitive areas in targeted observation for predicting the upstream Kuroshio transport variation. As stated in Eq. (2), the constraint scheme contains both the kinetic energy and the potential energy of the perturbation and fully considers all possible factors affecting the LM. Therefore, the scheme in Eq. (2) is utilized to identify the sensitive areas in this study, but here $(u', v', t', s', h')$ in Eq. (2) refer to the CNOP-type errors.

Similar to the method used in previous studies (Mu et al., 2009; Wang et al., 2013b), the vertically integrated total energy is ranked from large to small, and the areas with larger energy are defined as the sensitive areas for targeted observation. Of course, larger sensitive areas lead to better prediction results, but the economic cost of deploying observations over larger sensitive areas is correspondingly greater. To balance these considerations, 900 model grid points are selected, accounting for approximately 0.55% of all grid points, and almost covering the areas
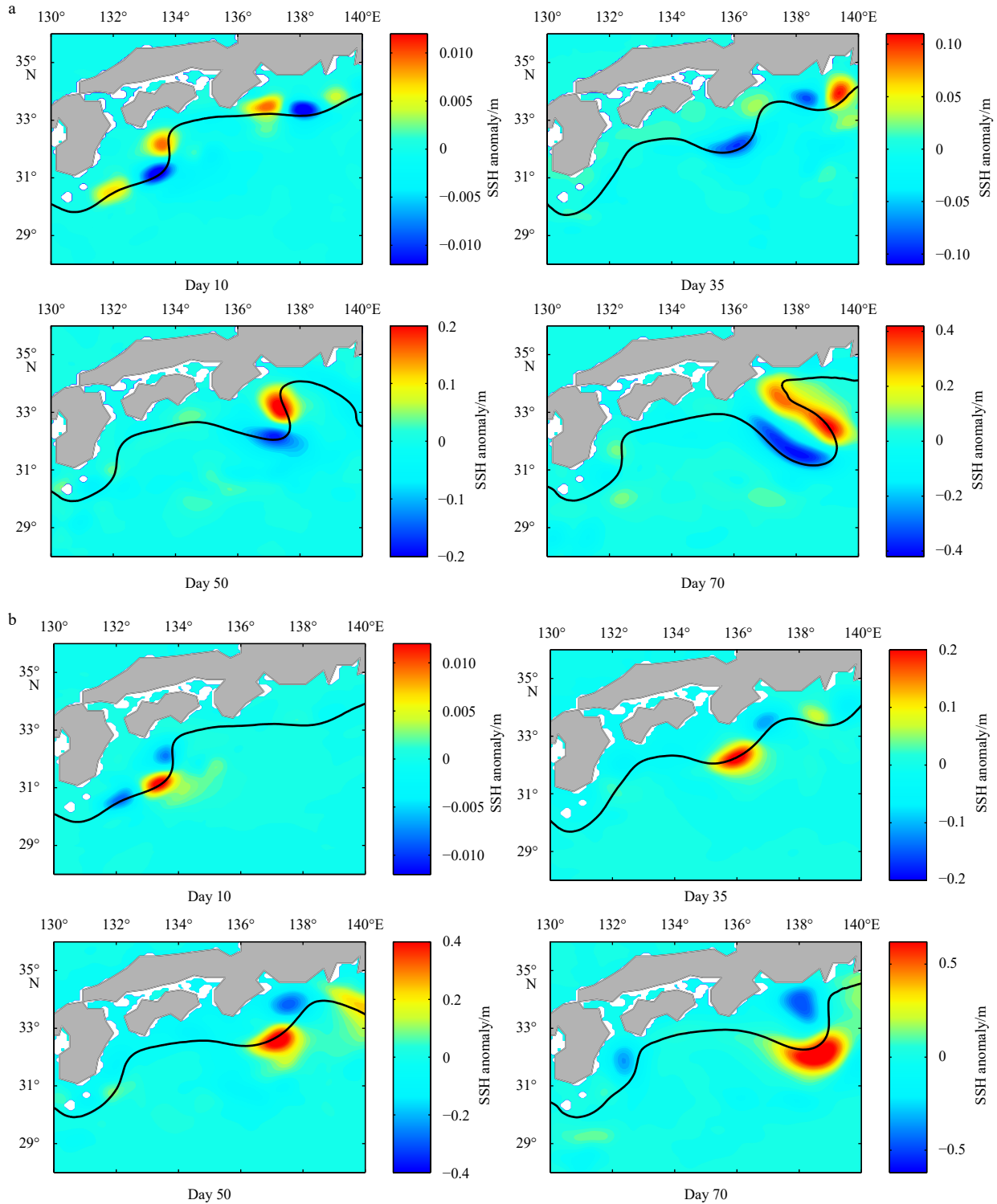
**Fig. 5.** Evolution of the sea surface height (SSH) anomaly component in the CNOP-type error field for Case 1: CNOP1 (a) and CNOP2 (b). The thick black line is the Kuroshio axis.

where the greatest energy is located.

Following the above steps, the identified sensitive areas in Case 1 and Case 2 are shown in Fig. 7. The sensitive areas for the two cases are similar, and both are located in the upstream region of the LM path, namely 29°–32°N, 131°–134°E. To verify the effectiveness of these sensitive areas, two sets of sensitivity experiments are designed: one is to investigate the effect of the spatial

positions of initial errors on the LM prediction, while the other is to evaluate the effect of the spatial structure of initial errors in the determined sensitive areas on the LM prediction.

### 3.2.2 *Sensitivity experiments*

Studies (Tsujino et al., 2006; Usui et al., 2008; Miyazawa et al., 2008; Xia et al., 2013; Wang et al., 2013b, c; Yang and Liang, 2019)
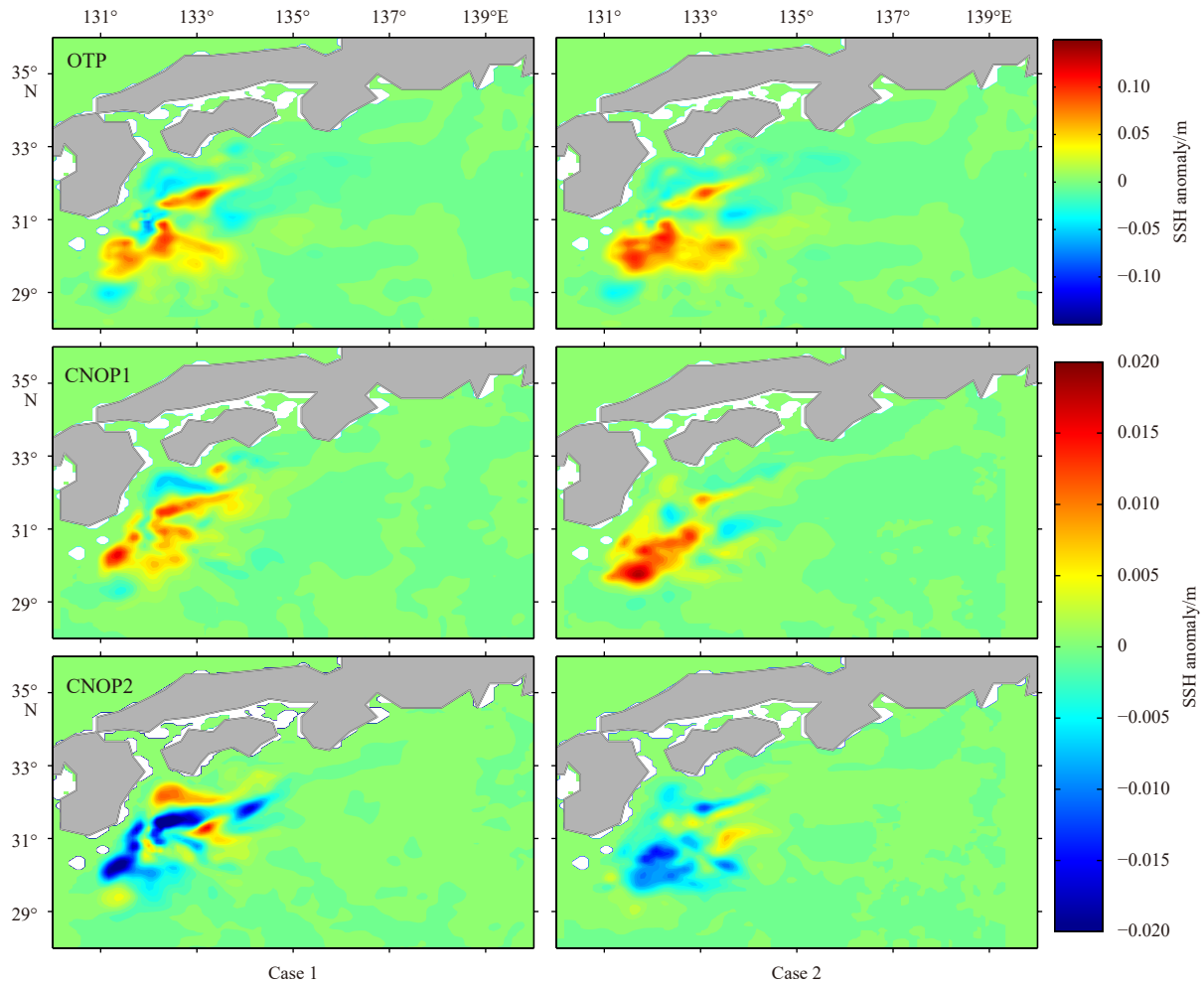
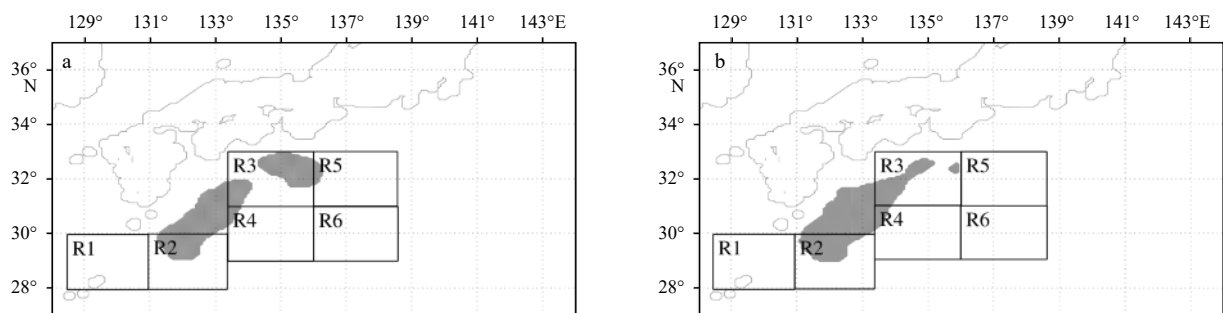**Fig. 6.** SSH anomaly components of the OTP and OIEs for two cases.



**Fig. 7.** Sensitive areas (shaded): Case 1 (a); Case 2 (b). R1–R6 are selected for comparison with the sensitive areas.

have suggested that the trigger meander southeast of Kyushu, the eddy interaction in the Shikoku recirculation region and the initial errors in the upstream region are strongly related to the LM formation. Therefore, the areas in the black boxes in Fig. 7 (denoted R1, R2, R3, R4, R5, and R6) with the same size as the sensitive areas are selected to investigate whether they are sensitive in ROMS. It should be noted that the areas north of R2 are almost included in the sensitive areas, and the sensitive areas have been compared with R1–R6; for convenience, the areas are not selected as comparison. Then in each area, 20 random errors satisfying the same constraint as the CNOP-type errors are generated as follows. All variables at each grid point for each specific area are

assigned random numbers, while the variables at the grid points in the other areas are set to zero. The random numbers are selected from a matrix that satisfies a normal distribution $N(0, \sigma)$, where $\sigma$ is selected randomly from 0 to 1. In addition, considering the accuracy of the observational instruments, the amplitude of the random numbers is set to 0.1.

As a measure of the prediction errors caused by the 20 random errors, their kinetic energies in the upper 1 000 m over the area 25°–35°N, 135°–140°E are presented in Figs 8–10. The random errors in these sensitive areas lead to the largest prediction errors. In addition, it is found from Fig. 9 that in Case 1, the prediction errors caused by random errors in R2 and R3 seem to be
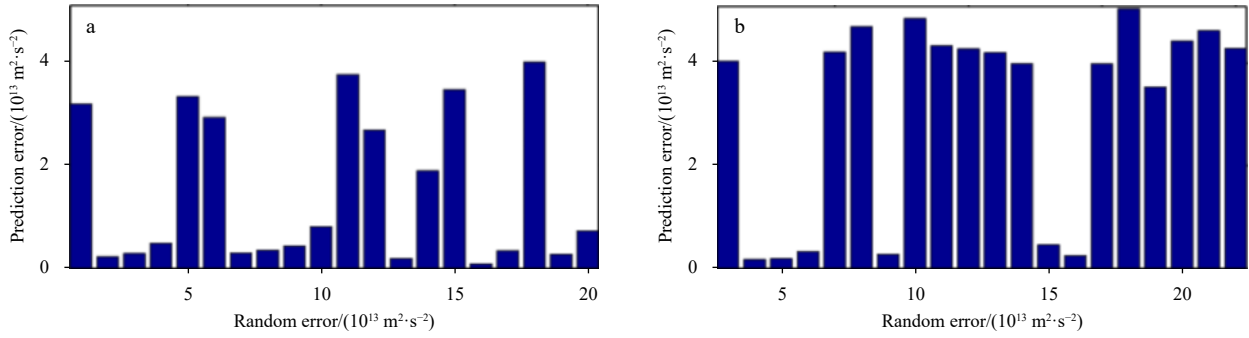
**Fig. 8.**  Prediction errors caused by random errors in the sensitive areas: Case 1 (a); Case 2 (b).
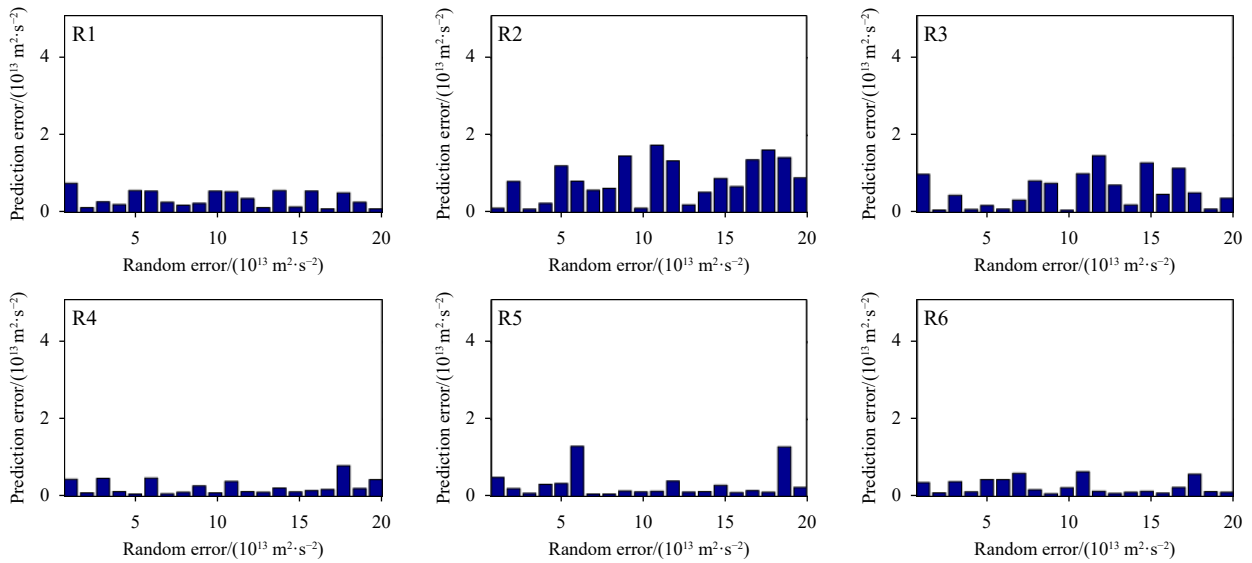


**Fig. 9.**  Prediction errors caused by random errors in R1–R6 for Case 1.
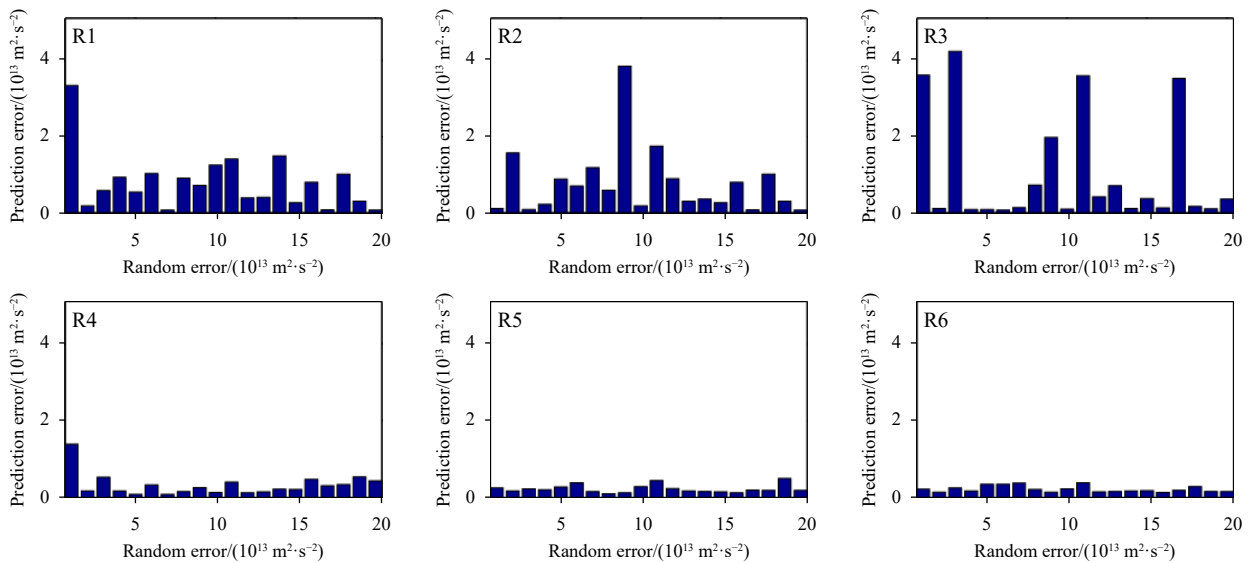


**Fig. 10.**  Prediction errors caused by random errors in R1–R6 for Case 2.

larger than those in R1, R4, R5, and R6. A similar result can be obtained for Case 2 (Fig. 10). This outcome is because R2 and R3 both partly cover sensitive areas (Fig. 7). For further quantitative analysis, the mean prediction errors caused by the 20 random er-

rors in different areas are listed in Table 2. The prediction errors caused by the random errors in the sensitive areas are 2–10 times larger than those caused by the random errors in R1–R6, and the prediction errors caused by the random errors in R2 and R3 are

**Table 2.** Mean prediction errors caused by the 20 random errors in sensitive areas and R1–R6 (unit: $10^{12}$ m²/s²)

| Event | Sensitive areas | R1 | R2 | R3 | R4 | R5 | R6 |
|-------|-----------------|------|------|-------|------|------|------|
| Case 1 | 14.83 | 3.46 | 8.31 | 5.50 | 2.47 | 3.02 | 2.55 |
| Case 2 | 31.07 | 7.95 | 7.67 | 10.37 | 3.20 | 2.22 | 2.08 |

approximately 2–4 times larger than those caused by the random errors in R1, R4, R5 and R6. These results indicate that the initial errors in the sensitive areas can develop faster than those at random locations, and that the spatial positions of the initial errors are important in LM prediction.

On the other hand, to investigate the effect of the spatial structure of initial errors in the sensitive areas on the LM prediction, it is started with the following questions: does the spatial structure of initial errors affect the LM prediction? If so, what spatial structure of initial errors can develop rapidly in sensitive areas?

To answer the above questions, 20 random errors are superimposed in the sensitive areas at the initial time; the constraint radius is the same as that of the CNOP-type errors reserved in the sensitive areas. Note that the sensitive areas are the regions with large CNOP amplitudes, that is to say, the errors reserved in the sensitive areas are just part of the CNOP-type errors. Therefore, it is necessary to examine the effect of the spatial structure of initial errors in the sensitive areas on the LM prediction. Then, the nonlinear model is integrated forward to the prediction time. The mean prediction errors caused by the 20 random errors in Case 1 and Case 2 are shown in Table 3. For Case 1, the prediction errors caused by the reserved CNOP-type errors is approximately 24 times larger than the prediction errors caused by random errors without specific spatial structure. For Case 2, the prediction errors caused by the reserved CNOP-type errors is approximately 15 times larger than the prediction errors caused by random errors. This demonstrates that the CNOP-type errors reserved in the sensitive areas develop faster than the random errors, implying that the spatial structure of initial errors has an important impact on the LM prediction.

Moreover, five errors are randomly selected from the above-

**Table 3.** Prediction errors caused by the 20 random errors and CNOP-type errors reserved in the sensitive areas (unit: $10^{12}$ m²/s²)

| Events | Prediction errors (CNOP-type) | Averaged results (20 random errors) |
|--------|-------------------------------|--------------------------------------|
| Case 1 | 19.51 | 0.81 |
| Case 2 | 13.69 | 0.95 |

mentioned random errors. By gradually increasing the similarity coefficient with the reserved CNOP-type errors from 0 to 1, five sets of errors with a specific spatial structure are obtained. Their relationship to the CNOP-type errors varies as follows:

$$\text{Error } i = \alpha \text{Error}_{\text{CNOP}} + (1-\alpha)\text{Error}_{\text{random}}, \alpha = 0.1, 0.2, \cdots, 1, \quad (4)$$

where the five sets of errors are denoted Error 1, Error 2, Error 3, Error 4, and Error 5. Each set includes 10 errors with different spatial structures, and their constraint radius is consistent with the CNOP-type error reserved in the sensitive areas. Then, each of these initial errors is superimposed in the sensitive areas onto the initial field to examine their influence on the prediction results. In Fig. 11, the vertical axis denotes the prediction errors caused by the initial errors at the prediction time, and the horizontal axis represents the similarity coefficient between the initial errors and the reserved CNOP-type errors. As the similarity coefficient increases, the prediction errors also increase with an approximately linear relationship. In other words, the initial errors that are more similar to the reserved CNOP-type errors have greater effects on the LM prediction. However, it should be noted that in Case 2, the prediction errors are less sensitive to the initial errors when the similarity coefficients are larger than 0.8, which may be related to the background state (the black line in Fig. 4). The LM path in the background state in Case 2 is toward the southwest, stronger than that in Case 1, which easily leads to the underestimation of the prediction errors. Moreover, five errors are randomly selected, and their evolution in the ocean model is also affected by nonlinearity. Therefore, the deviations in Case 2 are acceptable, and then it is speculated that prediction errors are caused mainly by the error component with the CNOP-type structure in the sensitive areas. This indicates that if the initial errors with the CNOP-type structure are reduced, the LM prediction result will be greatly improved.

In general, sensitivity experiments examine the effects of the spatial positions and spatial structure of initial errors on LM prediction and verify the validity of the sensitive areas defined based on the spatial structure of the OIEs. However, to better apply this conclusion to field-deployed observations, it is necessary to evaluate the effect of targeted observation in the sensitive areas.

### 3.2.3 *Observing system simulation experiment*

In this subsection, observing system simulation experiments (OSSEs) is adopted to evaluate the effect of targeted observation in the sensitive areas. In OSSEs, the observation data assimilated into a numerical model refer to the model simulation data (also
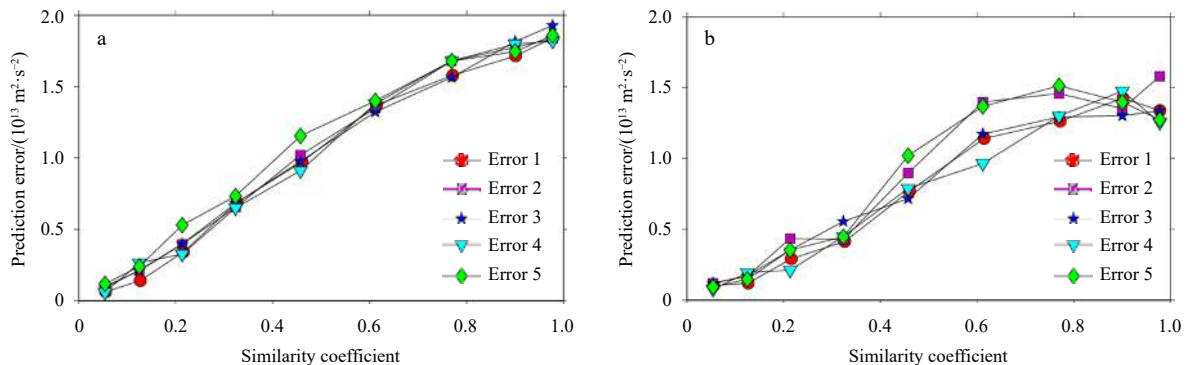


**Fig. 11.** Relationships between the similarity coefficients (between the initial errors and the CNOP-type errors reserved in the sensitive areas) and the prediction errors: Case 1 (a); Case 2 (b).

called the quasi-observation data). More importantly, OSSEs have been widely used in the atmospheric and ocean sciences, including for typhoon prediction (Qin and Mu, 2011), gulf stream prediction (Halliwell et al., 2014), South China Sea circulation prediction (Li et al., 2014), and upstream Kuroshio transport prediction (Zhang et al., 2017).

OSSEs are known as identical twin experiments and are divided into three steps: (1) initializing the ocean without errors and then integrating the nonlinear model from the initial time to the prediction time to generate the "truth" field, which is called the "nature run"; (2) superimposing errors on the initial field to obtain the new initial field and then integrating the nonlinear model forward to the prediction time, which is called the "control run"; and (3) applying additional observations to the sensitive areas and then assimilating the quasi-observation data into the initial field of the control run to eliminate the initial errors as much as possible, which is called the "targeted run". It should be noted that the initial errors are superimposed onto the whole initial field in the control run but not in the targeted run. Then, the initial errors in sensitive areas are eliminated by targeted observation. Comparing the results in the control run and targeted run with those in the nature run, two sets of prediction errors are obtained. Then, the effectiveness of targeted observation is examined by investigating the prediction errors.

In the control run of the OSSEs, the differences between the model outputs of two adjacent months are taken as the analysis errors. For the analysis errors with less influence on the LM prediction, even if a targeted observation is implemented in the sensitive areas, the prediction improvement may not be great. Therefore, to more reasonably evaluate the effectiveness of targeted observation, 20 analysis errors that lead to greater prediction errors for Case 1 and Case 2 are selected. Then, in the targeted run, the initial state in the sensitive areas is improved using the quasi-observation data to examine the prediction improvement. In this study, the quasi-observation data refer to the ROMS simulation outputs. The initial field in the sensitive areas is directly replaced by quasi-observation data, successfully excluding the influence of the data assimilation method. However, it is impossible to completely remove the errors even with the addition of observations, so a few random errors with a magnitude of 0.01 are reserved in the sensitive areas. For comparison, similar treatments were applied to R1, R2, R3, R4, R5, and R6. In addition, the kinetic energy caused by the errors above 1 000 m in the verification area (25°–35°N, 135°–140°E) is used to measure the prediction result, consistent with the objective function in Eq. (3). Therefore, the smaller the kinetic energy is at the verification time, the better the prediction result.

In this paper, the prediction improvement is defined as follows:

$$\text{Improvement} = \frac{KE1 - KE2}{KE1} \times 100\% , \qquad (5)$$

where $KE1$ indicates the prediction errors in the control run and $KE2$ refers to the prediction errors in the targeted run. For the 20 initial errors mentioned above, the mean prediction improvements after targeted observation in different areas are listed in Tables 4 and 5. Case 1 is taken as an example for analysis. These two tables demonstrate that the prediction results are improved by nearly 27% after assimilating targeted observations in the sensitive areas; this improvement is far greater than the effects of targeted observation in R1–R6. Because R2 covers some of the sensitive areas, eliminating the initial errors in R2 improves the

**Table 4.** Mean prediction improvements caused by the 20 initial errors after performing targeted observation for Case 1

|  | Sensitive areas | R1 | R2 | R3 | R4 | R5 | R6 |
|---|---|---|---|---|---|---|---|
| Improvement (mean) | 26.92% | 4.88% | 21.71% | 6.28% | −3.14% | 5.51% | 3.77% |

**Table 5.** Mean prediction improvements caused by the 20 initial errors after performing targeted observation for Case 2

|  | Sensitive areas | R1 | R2 | R3 | R4 | R5 | R6 |
|---|---|---|---|---|---|---|---|
| Improvement (mean) | 17.61% | 4.83% | 11.85% | 3.97% | 1.17% | −0.61% | 2.05% |

prediction results by approximately 21%, but the prediction improvements in the other five areas are less than 5%. This is consistent with the conclusion obtained in the sensitivity experiment. In addition, it is found that targeted observation in any random area will not necessarily improve the prediction results. For example, implementing targeted observations in R4 leads to worse results, with a 3.14% reduction in the prediction skill. This implies that although the initial errors are observed and reduced in other areas, the prediction skill of the LM path is not improved and may even worsen. For Case 2, a similar conclusion is drawn.

The OSSEs reveal that when targeted observations are implemented in the sensitive areas, the prediction errors are effectively reduced, and the prediction skill is improved significantly. This not only confirms the validity of the sensitive areas but also provides scientific guidance for field-deployed observations.

## 4 Conclusions

In this paper, the ROMS model with realistic bottom topography was adopted to reproduce the Kuroshio path variations south of Japan using a one-way nested simulation. The model succeeded in capturing the essential characteristics of the LM event under climatological forcing. The CNOP method was used to investigate the sensitive areas in targeted observation for predicting the Kuroshio LM path. To seek the OIEs existing along with the triggering signal, the LM events caused by the OTP were selected as a new background state. With the obtained OIEs, which can lead to the largest prediction errors in the LM prediction, the sensitive areas were determined and evaluated through OSSEs.

This study indicated that two types of OIEs (CNOP1 and CNOP2) for Case 1 and Case 2 are concentrated mainly to the southeast of Kyushu. CNOP1 tended to overestimate the intensity of the predicted LM while CNOP2, featuring a negative correlation with CNOP1, tended to underestimate the LM path. However, both cases exhibited uniform localization and spatial structures, and a certain similar relationship existed between the OIEs in the LM prediction and the OTP of the LM path. This helped us identify the sensitive areas in targeted observation for predicting the LM path, which were located in the area of 29°–32°N, 131°–134°E. This findings confirmed that in these sensitive areas, the initial errors could develop faster than errors in random positions. In addition, the initial errors with the CNOP-type structure in the sensitive areas could evolve faster than those without a specific spatial structure. Therefore, the identified sensitive areas based on the spatial structures of OIEs were effective. After the initial errors in the sensitive areas were reduced, the prediction skills were effectively improved, thereby affirming the effect of implementing targeted observation on the LM prediction.

This study constitutes the first attempt to identify the sensitive areas for predicting the LM path in a complex regional ocean model. The findings confirm the importance of the areas southeast of Kyushu in predicting the LM path, which is consistent with the conclusions of previous studies regarding LM formation (Tsujino et al., 2006; Usui et al., 2008; Miyazawa et al., 2008). However, considering the limitations in observation data and computing resources, this work on targeted observation is relatively preliminary. To apply the results to real-time observations, there is still much work to be done. For example, the OIEs are mostly concentrated in the upper 2 500 m, and how to design the optimal observation network and determine the optimal locations of instruments needs to be explored in the future.

## References

Farrara J D, Chao Yi, Li Zhijin, et al. 2013. A data-assimilative ocean forecasting system for the Prince William sound and an evaluation of its performance during sound Predictions 2009. Continental Shelf Research, 63(S1): S193–S208, doi: 10.1016/j.csr.2012.11.008

Fujii Y, Tsujino H, Usui N, et al. 2008. Application of singular vector analysis to the Kuroshio large meander. Journal of Geophysical Research: Oceans, 113(C7): C07026, doi: 10.1029/2007JC004476

Halliwell Jr R G, Srinivasan A, Kourafalou V, et al. 2014. Rigorous evaluation of a fraternal twin ocean OSSE system for the open Gulf of Mexico. Journal of Atmospheric and Oceanic Technology, 31(1): 105–130, doi: 10.1175/JTECH-D-13-00011.1

Hayasaki M, Kawamura R, Mori M, et al. 2013. Response of extratropical cyclone activity to the Kuroshio large meander in northern winter. Geophysical Research Letters, 40(11): 2851–2855, doi: 10.1002/grl.50546

Ishikawa Y, Awaji T, Komori N, et al. 2004. Application of sensitivity analysis using an adjoint model for short-range forecasts of the Kuroshio path south of Japan. Journal of Oceanography, 60(2): 293–301, doi: 10.1023/b:joce.0000038335.50080.ff

Kawabe M. 1995. Variations of current path, velocity, and volume transport of the Kuroshio in relation with the large meander. Journal of Physical Oceanography, 25(12): 3103–3117, doi: 10.1175/1520-0485(1995)025<3103:VOCPVA>2.0.CO;2

Langland R H. 2005. Issues in targeted observing. Quarterly Journal of the Royal Meteorological Society, 131(613): 3409–3425, doi: 10.1256/qj.05.130

Li Yineng, Peng Shiqiu, Liu Duanling. 2014. Adaptive observation in the South China Sea using CNOP approach based on a 3-D ocean circulation model and its adjoint model. Journal of Geophysical Research: Oceans, 119(12): 8973–8986, doi: 10.1002/2014JC010220

Liu Xia, Mu Mu, Wang Qiang. 2018a. The nonlinear optimal triggering perturbation of the Kuroshio large meander and its evolution in a regional ocean model. Journal of Physical Oceanography, 48(8): 1771–1786, doi: 10.1175/JPO-D-17-0246.1

Liu Xia, Wang Qiang, Mu Mu. 2018b. Optimal initial error growth in the prediction of the Kuroshio large meander based on a high-resolution regional ocean model. Advances in Atmospheric Sciences, 35(11): 1362–1371, doi: 10.1007/s00376-018-8003-z

Ma Xiaohui, Jing Zhao, Chang Ping, et al. 2016. Western boundary currents regulated by interaction between ocean eddies and the atmosphere. Nature, 535(7613): 533–537, doi: 10.1038/nature18640

Miyazawa Y, Kagimoto T, Guo Xinyu, et al. 2008. The Kuroshio large meander formation in 2004 analyzed by an eddy-resolving ocean forecast system. Journal of Geophysical Research: Oceans, 113(C10): C10015, doi: 10.1029/2007JC004226

Miyazawa Y, Yamane S, Guo Xinyu, et al. 2005. Ensemble forecast of the Kuroshio meandering. Journal of Geophysical Research: Oceans, 110(C10): C10026, doi: 10.1029/2004JC002426

Mu Mu. 2013. Methods, current status, and prospect of targeted observation. Science China: Earth Sciences, 56(12): 1997–2005, doi: 10.1007/s11430-013-4727-x

Mu Mu, Duan Wansuo, Wang B. 2003. Conditional nonlinear optimal perturbation and its applications. Nonlinear Processes in Geophysics, 10(6): 493–501, doi: 10.5194/npg-10-493-2003

Mu Mu, Zhou Feifan, Wang Hongli. 2009. A method for identifying the sensitive areas in targeted observations for tropical cyclone prediction: conditional nonlinear optimal perturbation. Monthly Weather Review, 137(5): 1623–1639, doi: 10.1175/2008MWR2640.1

Nakamura H, Nishina A, Minobe S. 2012. Response of storm tracks to bimodal Kuroshio path states south of Japan. Journal of Climate, 25(21): 7772–7779, doi: 10.1175/JCLI-D-12-00326.1

Qin Xiaohao, Mu Mu. 2011. A study on the reduction of forecast error variance by three adaptive observation approaches for tropical cyclone prediction. Monthly Weather Review, 139(7): 2218–2232, doi: 10.1175/2010MWR3327.1

Shao Quanqin, Ma Weiwei, Chen Zhuoqi, et al. 2005. Relationship between Kuroshio meander pattern and Ommastrephes bartrami CPUE in northwest Pacific Ocean. Oceanologia et Limnologia Sinica, 36(2): 111–122

Shchepetkin A F, McWilliams J C. 2003. A method for computing horizontal pressure-gradient force in an oceanic model with a nonaligned vertical coordinate. Journal of Geophysical Research: Oceans, 108(C3): 3090, doi: 10.1029/2001JC001047

Shchepetkin A F, McWilliams J C. 2005. The regional oceanic modeling system (ROMS): a split-explicit, free-surface, topography-following-coordinate oceanic model. Ocean Modelling, 9(4): 347–404, doi: 10.1016/j.ocemod.2004.08.002

Song Yuhe, Haidvogel D. 1994. A semi-implicit ocean circulation model using a generalized topography-following coordinate system. Journal of Computational Physics, 115(1): 228–244, doi: 10.1006/jcph.1994.1189

Taft B A. 1972. Characteristics of the flow of the Kuroshio south of Japan. In: Stommel H, Yoshida K, eds. Kuroshio-Its Physical Aspects. Tokyo, Japan: University of Tokyo Press, 165–216

Tang Youmin, Kleeman R, Moore A M. 2004. SST assimilation experiments in a tropical Pacific Ocean model. Journal of Physical Oceanography, 34(3): 623–642, doi: 10.1175/3518.1

Tsujino H, Usui N, Nakano H. 2006. Dynamics of Kuroshio path variations in a high-resolution general circulation model. Journal of Geophysical Research: Oceans, 111(C11): C11001, doi: 10.1029/2005JC003118

Usui N, Tsujino H, Nakano H. 2008. Formation process of the Kuroshio large meander in 2004. Journal of Geophysical Research: Oceans, 113(C8): C08047, doi: 10.1029/2007JC004675

Wang Qiang, Ma Libin, Xu Qiangqiang. 2013a. Optimal precursor of the transition from Kuroshio large meander to straight path. Chinese Journal of Oceanology and Limnology, 31(5): 1153–1161, doi: 10.1007/s00343-013-2301-1

Wang Qiang, Mu Mu, Dijkstra H A. 2012. Application of the conditional nonlinear optimal perturbation method to the predictability study of the Kuroshio large meander. Advances in Atmospheric Sciences, 29(1): 118–134, doi: 10.1007/s00376-011-0199-0

Wang Qiang, Mu Mu, Dijkstra H A. 2013b. The similarity between optimal precursor and optimally growing initial error in prediction of Kuroshio large meander and its application to targeted observation. Journal of Geophysical Research: Oceans, 118(2): 869–884, doi: 10.1002/jgrc.20084

Wang Qiang, Mu Mu, Dijkstra H A. 2013c. Effects of nonlinear physical processes on optimal error growth in predictability experiments of the Kuroshio Large Meander. Journal of Geophysical Research: Oceans, 118(12): 6425–6436, doi: 10.1002/2013JC009276

Xia Ruibin, Liu Qinyu, Xu Lixiao. 2013. Formation mechanisms of the three Kuroshio large meanders. Periodical of Ocean University of China, 43(5): 1–7

Xu Haiming, Tokinaga H, Xie Shangping. 2010. Atmospheric effects of the Kuroshio large meander during 2004–05. Journal of Climate, 23(17): 4704–4715, doi: 10.1175/2010JCLI3267.1

Yang Yang, Liang Xiangsan. 2019. New perspectives on the generation and maintenance of the Kuroshio large meander. Journal of Physical Oceanography, 49(8): 2095–2113, doi: 10.1175/JPO-D-18-0276.1

Zhang Kun, Mu Mu, Wang Qiang. 2017. Identifying the sensitive area in adaptive observation for predicting the upstream Kuroshio transport variation in a 3-D ocean model. Science China: Earth Sciences, 60(5): 866–875, doi: 10.1007/s11430-016-9020-8

Zou Guangan, Wang Qiang, Mu Mu. 2016. Identifying sensitive areas of adaptive observations for prediction of the Kuroshio large meander using a shallow-water model. Chinese Journal of Oceanology and Limnology, 34(5): 1122–1133, doi: 10.1007/s00343-016-4264-5